Supplementary information

Nitrogen cycle on N-doped graphene loaded TiO_2 for efficient photocatalytic dinitrogen conversion

Shuaikang Sang,†[a] Keke Mao,†[b] Dawei Xi,†[a] Wenbin Jiang,[a] Zeming Qi,[a] Yang Pan,[a] Hui Zhang,[cd] Zhi Liu,[cd] Jingxiang Low,*[e] Ran Long,*[a] Yujie Xiong*[a]

[a] *Hefei National Research Center for Physical Sciences at the Microscale, School of Chemistry and Materials Science, and National Synchrotron Radiation Laboratory, University of Science and Technology of China, Hefei, Anhui, 230026, China. E-mail: longran@ustc.edu.cn; yjxiong@ustc.edu.cn.*

[b] *School of Energy and Environment Science, Anhui University of Technology, Maanshan, Anhui 243032, China.*

[c] *School of Physical Science and Technology, ShanghaiTech University, Shanghai 201203, China.*

[d] *State Key Laboratory of Functional Materials for Informatics, Shanghai Institute of Microsystem and Information Technology, Chinese Academy of Sciences, Shanghai 200050, China.*

[e] *School of Physical Science and Technology, Tiangong University, Tianjin 300387, China. E-mail: jxlow@tiangong.edu.cn.*

†These authors contributed equally to this work.

S1. Experimental details

S1.1. Sample preparation

S1.1.1. Materials

The chemical reagents purchased from Shanghai Chemical Reagent Factory (Shanghai, China) were used throughout all experiments without further purification.

S1.1.2. Preparation of rutile TiO_2/graphene composite

The rutile TiO_2/graphene (rutile/G) was prepared through chemical vapor deposition method.[1] In a typical procedure, 500 mg commercial rutile TiO_2 was spread in a horizontal quartz tube. Then, the quart tube was placed in a tubular furnace and calcined at 700 °C with a ramping rate of 10 °C min^{-1} in dinitrogen atmosphere. When the temperature reached 700 °C, 0.5 mL benzene was injected into tubular furnace using a 2 mL syringe attached on a syringe pump for 30 min. After heating at 700 °C for 2 h, the system was cooled to ambient temperature. Finally, the samples was ground and collected.

S1.2. Characterization

The phase structures of the prepared samples were determined via a D/Max-RB X-ray diffractometer (XRD) (Rigaku, Japan) using CuKα radiation ($\lambda = 0.15418$ nm) with a scan rate of 0.05° s^{-1}. The transmission electron microscopy (TEM) images were taken on Hitachi Model H-7700 microscope operated at 100 kV. X-ray photoelectron spectroscopy (XPS) characterization of the prepared samples was carried out on JPS-9010MC (JEOL, Japan) with a hemispherical electron energy analyzer (1486 eV Al Kα radiation). During the XPS characterization, the binding energy of all prepared samples was calibrated with the C 1s peak of adventitious carbon (284.5 eV). Raman spectrometer (Renishaw InVia, UK) with back-scattering geometry and 514.5 nm laser excitation was used to perform Raman analysis. Fourier-transform infrared spectroscopy (FTIR) characterization was performed in the transmittance mode using an FTIR spectrometer (Nicolet 6700, ThermoFisher, USA). The optical properties of the prepared samples were studied by investigating their light absorption spectra obtained on a UV-visible spectrophotometer (UV-3600, Shimadzu, Japan). The reflectance reference for the UV-visible spectrophotometer was $BaSO_4$. Brunauer–Emmett–Teller (BET) specific surface area (S_{BET}) of the prepared samples was obtained using nitrogen adsorption-desorption isotherm obtained on a Micromeritics ASAP 2020 nitrogen adsorption apparatus (USA) through a multipoint BET method using the adsorption data at the relative pressure (P/P_0) range of 0.05–0.3. The samples were degassed at 180 °C before the test. The Barret-Joyner-Halender (BJH) method was used to estimate the pore size distribution of the prepared samples. The pore volume and average pore size of the prepared samples were investigated using the adsorbed nitrogen volume at the relative pressure (P/P_0) of 0.994. N K-edge XAS studies for the prepared samples were carried out at the beamline BL12B-a of National Synchrotron Radiation Laboratory (NSRL) in Hefei, China. A 800 MeV electron beam energy from the storage ring with an average current of 300 mA was applied throughout the test. A bending magnet was linked to the beamline and equipped with three gratings covering photon energies from 100 to 1000 eV with an energy resolution of ~0.2 eV. The results were obtained in the TEY mode via recording the drain current for the samples at a vacuum greater than 5×10^{-8} Pa.

S1.3. Electrochemical measurement and photocatalytic performance test

Electrochemical photocurrent and impedance spectroscopy studies of the prepared samples were measured on a standard three-electrode electrochemical analyzer

(CHI660C instruments, CHI, China) system. The light source for these tests was a low power UV-LED (3 W, 365 nm). 30 mL 0.5 M Na_2SO_4 aqueous solution was used as an electrolyte throughout the electrochemical test. The prepared samples coated on FTO with a geometrical area of 1.0 cm^2, Pt wire and Ag/AgCl immersed in the filling solution (saturated KCl) were employed as working, counter and reference electrodes, respectively.

The photocatalytic nitrogen reduction test was performed in a home-made reactor. Generally, 10 mg sample was first dispersed in 15 mL deionized (DI) water and poured into the reactor. The dispersion was dried at 70 °C for 12 h, creating a thin film at the bottom of the reactor. Prior to the photocatalytic reaction, 1 mL DI water was added into the notch in the reactor. After purging the reactor with N_2 gas (flowing through the water) with a flow rate of 30 ml/min for 30 min, the reactor was irradiated by a 300 W Xe lamp (PLS-SXE300D, Beijing Perfectlight, China) for 2 h under stirring and N_2 gas flow. The power densities of light were measured to be 130 mW cm^{-2}. 20 mL of 0.2 mM H_2SO_4 solution was used to collect the exhaust gas from the reactor. Finally, the NH_4^+ concentration in the H_2SO_4 solution was detected through anion and cation chromatograph (IC 1040, Techcomp). Specifically, the NH_4^+ concentration in the H_2SO_4 solution was measured via cation chromatography. For NO detection, a similar procedure was followed, with the following modifications: (1) the reactor was sealed during the photocatalytic reaction, and (2) following the reaction, O_2 was introduced into the reactor for 30 min to oxidize the produced NO to NO_2, which is more water-soluble. The resulting gas mixture was then collected in 20 mL of 0.2 mM H_2SO_4 solution for subsequent analysis. The total product yield was calculated by multiplying the measured concentration by the volume of the test solution. To obtain the catalytic activity data, the total product yield was normalized by the reaction time of 2 h and catalyst mass of 10 mg.

The experimental procedure of the SVUV-PIMPS was similar to that of the photocatalytic nitrogen reduction test, except that the final products were analyzed using the SVUV-PIMPS system at BL04B beamline of the National Synchrotron Radiation Laboratory (NSRL) in Hefei. The photon energy of the SVUV-PIMS could be tuned from to avoid the fragments, allowing the precise determination of the products. With a photon energy of 11 eV, the NH_3 and NO can be detected without any fragments.

The in situ diffuse reflectance infrared Fourier transform spectra (DRIFTS) were collected using Bruker IFS 66v Fourier transformation spectrometer with a Harrick diffuse reflectance accessory at the Infrared Spectroscopy and Microspectroscopy Endstation (BL01B) in the National Synchrotron Radiation Laboratory (NSRL), Hefei. Prior to the test, the sample was placed into the reaction chamber of the DRIFTS. Then the chamber was purged with argon (99.999%) for 1 h to collect the background spectrum. Subsequently, the chamber was sealed and flowed with the dinitrogen gas and water vapor. The DRIFTS spectra were recorded under dark and light irradiation conditions. 365 nm LED (3 W, UV-LED1030, Zhenjiang SG-Tech) was used as the light source during the test. The spectra were then collected at 10, 20, and 30 min under both conditions. Each spectrum was collected with an average of 128 scans at a resolution of 2 cm^{-1}. Finally, the obtained spectra were subtracted by the background spectrum.

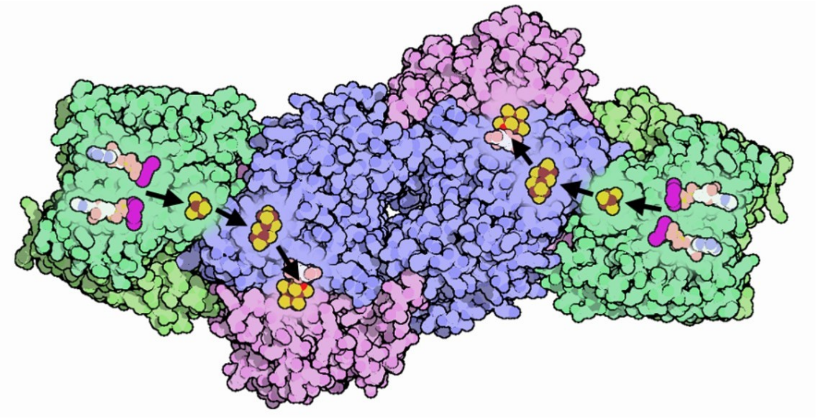

Figure S1. Schematic illustration for the charge carrier migration on the natural nitrogenase composing of Fe protein (green color section) and MoFe protein built by P-cluster (purple color section) and MoFe cluster (pink color section). Image from the RCSB PDB February 2002 Molecule of the Month feature by David Goodsell (doi:10.2210/rcsb_pdb/mom_2002_2).

In a typical natural nitrogenase system, two proteins are included which are MoFe protein and Fe protein. By consuming two molecules of ATP, electrons can be generated on the Fe protein. Then, these produced electrons on Fe protein can further migrate to the P-cluster of MoFe protein and then to the MoFe-cluster of MoFe protein. Finally, electrons can be utilized to reduce the nitrogen molecule adsorbed on the MoFe protein for producing ammonia.

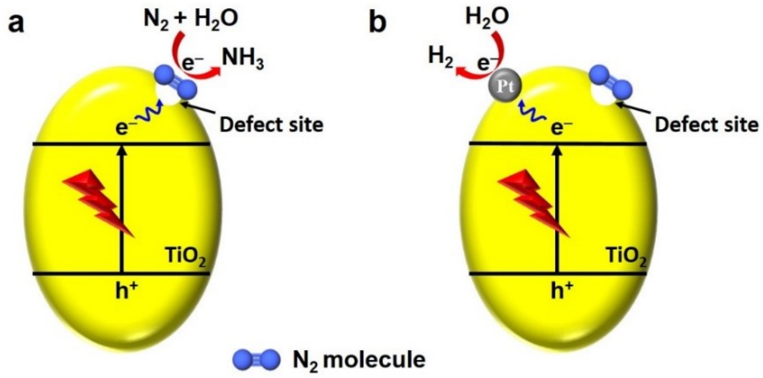

Figure S2. Schematic illustration for the photocatalytic dinitrogen fixation pathway on the (a) defect-modified semiconductor (*i.e.*, TiO_2) and (b) co-catalyst (*i.e.*, Pt nanoparticle) loaded defect-modified semiconductor (i.e., TiO_2).

Conventionally, the semiconductor and its surface defects are utilized as a light-harvesting unit and surface-active sites for photocatalytic dinitrogen fixation (Figure S2a). However, through this strategy, the cocatalyst, which has always been used for accelerating photogenerated charge carrier separation, can hardly be applied. In detail, photogenerated electrons tend to migrate to the cocatalyst instead of the surface defect sites on the semiconductor (Figure S2b). Therefore, the photogenerated electrons will be utilized for water splitting instead of dinitrogen reduction.

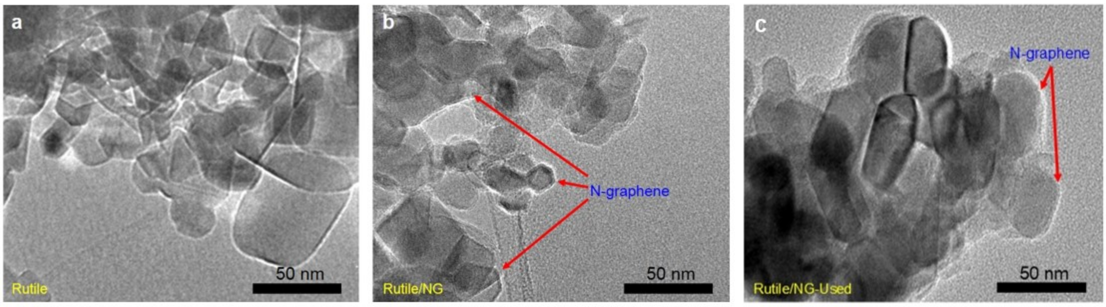

Figure S3. TEM images for (a) rutile and (b) rutile/NG (c) rutile/NG-Used.

Generally, the morphology of the prepared samples can be resolved by microscopy characterization, revealing that the rutile exhibits a spherical structure with a size of 20–50 nm (Figure S3a). In addition, as shown in Figure S3b, a thin rough sheath can be observed on the rutile nanoparticles (NPs) after loading of the NG on the rutile, manifesting the wrapping of NG on the rutile NPs. After the reaction, the rutile/NG structure remains unchanged (Figure S3c).

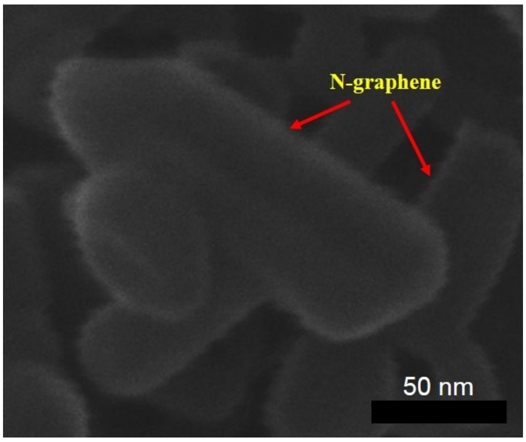

Figure S4. Scanning helium ion microscope image for the rutile/NG.

As revealed by scanning helium ion microscopy image of the rutile/NG, a thin rough sheath can be observed on the rutile nanoparticles after loading of the NG.

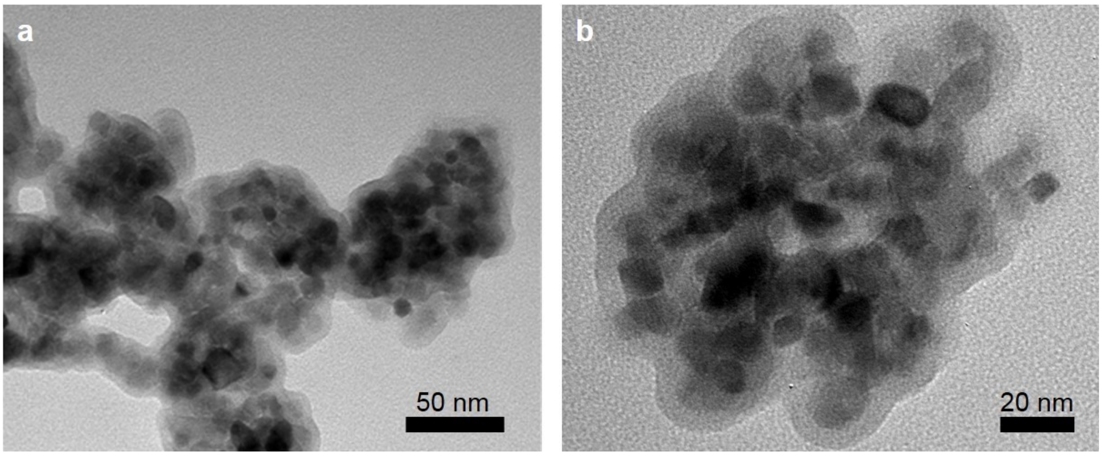

Figure S5. TEM images for the rutile/NG with high NG loading concentration, where 1 mL of pyridine was used during the sample preparation**.**

To further confirm the rough sheath is attributed to the NG, the dosage of the NG on rutile/NG is enormously increased and the TEM images of the resultant samples are shown in Figure S5. Obviously, with the increased NG dosage, the sheathes on the rutile NPs are further grown, indicating that the thickness of the surface sheath is proportional to the NG concentration. This result confirms that the NG is wrapped on the rutile, forming a sheath structure.

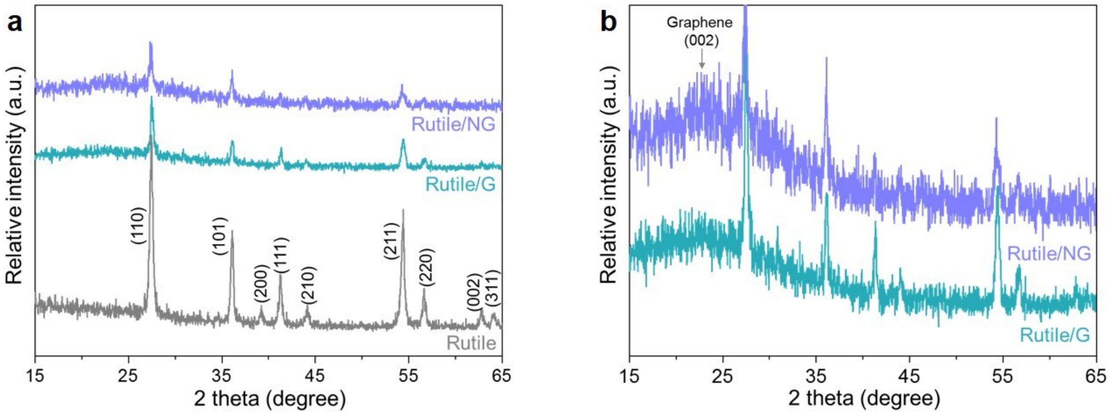

Figure S6. (a) XRD and (b) enlarged XRD diffraction patterns for the rutile, rutile/G and rutile/NG.

The crystallinity and phase structures of the prepared samples are investigated by X-ray diffraction as shown in Figure S6a. Apparently, all the prepared samples show diffraction peaks attributed to the rutile TiO_2. It should be noted that the intensity of the diffraction peaks attributed to the rutile TiO_2 is slightly reduced after loading of G and NG due to the shielding effect of G and N on the rutile TiO_2. This result suggests that the G and NG are uniformly distributed on the prepared samples. In addition, as shown in the magnified XRD patterns in Figure S6b, a broad diffraction peak at *ca*. 24° can be observed on the rutile/G and rutile/NG.[2] This extra peak is corresponding to the few layer graphene, indicating the successful loading of G and NG on the TiO_2.

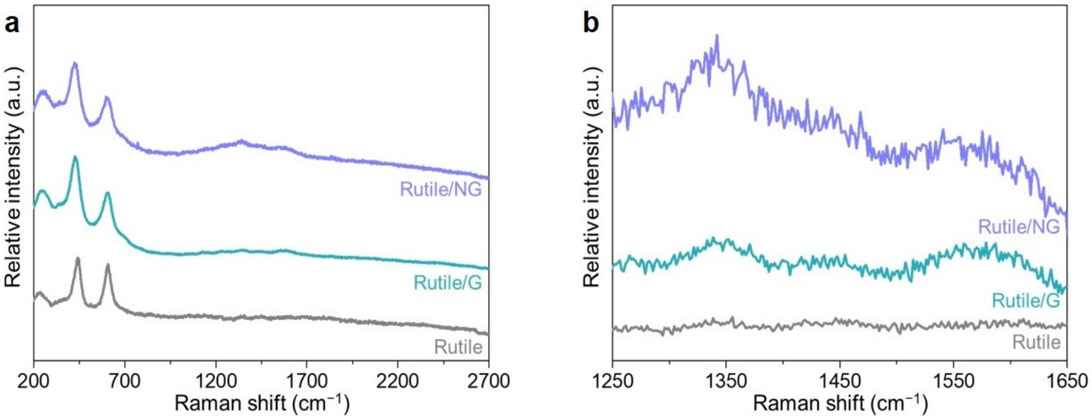

Figure S7. (a) Raman and (b) enlarged Raman spectra for the rutile, rutile/G and rutile/NG.

The defect density of the graphene loaded on the rutile is further investigated by Raman spectroscopy. Generally, the defect density on the graphene nanosheets can be reflected by its intensity ratio of their D- and G-bands, where the higher the I_D/I_G ratio, the higher the defect density on the graphene nanosheets.[3] Obviously, the I_D/I_G ratio of the rutile/NG is higher than that of the rutile/G. This result is easy to understand because the N-doping can create enormous defective sites on the graphene framework. The presence of defective sites on the NG attributed to the N-doping can be beneficial for nitrogen adsorption and activation.

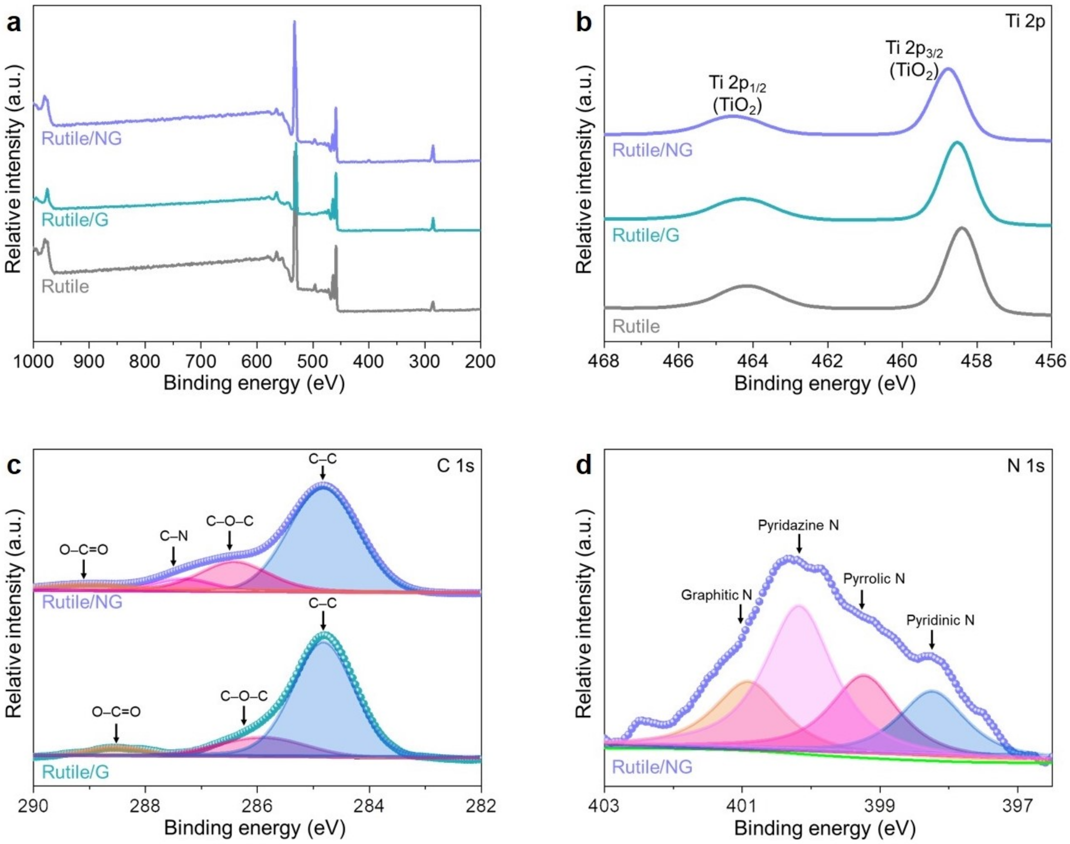

Figure S8. (a) Survey, (b) high-resolution Ti 2p, (c) high-resolution C 1s and (d) high-resolution N 1s XPS spectra for the prepared samples.

XPS characterization is carried out to determine the surface composition of the prepared samples. As shown in the survey spectra, all the prepared samples contain Ti, O and C elements (Figure S8a); whilst an additional peak at around 400 eV can be observed on the survey spectrum of the rutile/NG due to the N-doping. For the high-resolution Ti 2p XPS spectra (Figure S8b), two main peaks originating from the TiO_2 can be found on all prepared samples. In addition, C 1s XPS spectra of the rutile/G and rutile/NG reveal that an additional C–N peak can be found on rutile/NG due to the N-doping on the graphene (Figure S8c). Furthermore, the chemical status of the N-dopant on the rutile/NG can be studied via fitting its N 1s XPS spectrum (Figure S8d). The results reveal that the prepared N-doped graphene is mainly composed of pyridazine-N,[4, 5] accompanying by the traceable amount of pyridinic-N, pyrrolic-N and graphitic-N.[4, 6] These results are opposite to our subconscious understanding, where the pyridinic-N should be dominated in this NG structure which is prepared by employing pyridine as its precursor. In fact, the domination of the pyridazine-N is due to the rupture of the pyridine ring during the chemical vapor deposition. In detail, the C–H bond on the pyridine ring was more likely to be broken under high temperature (700 °C) due to its lowest bonding energy among C–H (102.4 kcal/mol), C–C (117.2 kcal/mol) and C–N (106.5 kcal/mol) bonds, forming two (HCN, C_2H_2 and C_2H_4) or four (C_2H_3NN, C_4H_2 and C_4H_4) heavy atom chains.[7, 8] Then, these atom chains can polymerize into the N-doped graphene.[9] In addition, the defect graphene prepared through this method owns enormous broken edge, which can be utilized for trapping the N_2 to create pyridazine sites,[10-12] further increasing the pyridazine density on the prepared samples.

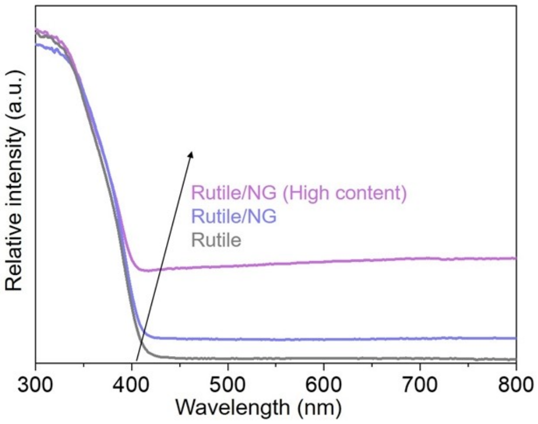

Figure S9. Light absorption spectra for the prepared samples.

As shown in Figure S9, all the prepared samples exhibit light absorption edges at *ca*. 400 nm due to the intrinsic light absorption of the rutile. In addition, an increase in visible-light absorption can be observed after loading of the NG due to the black color characteristic of the graphene.[13]

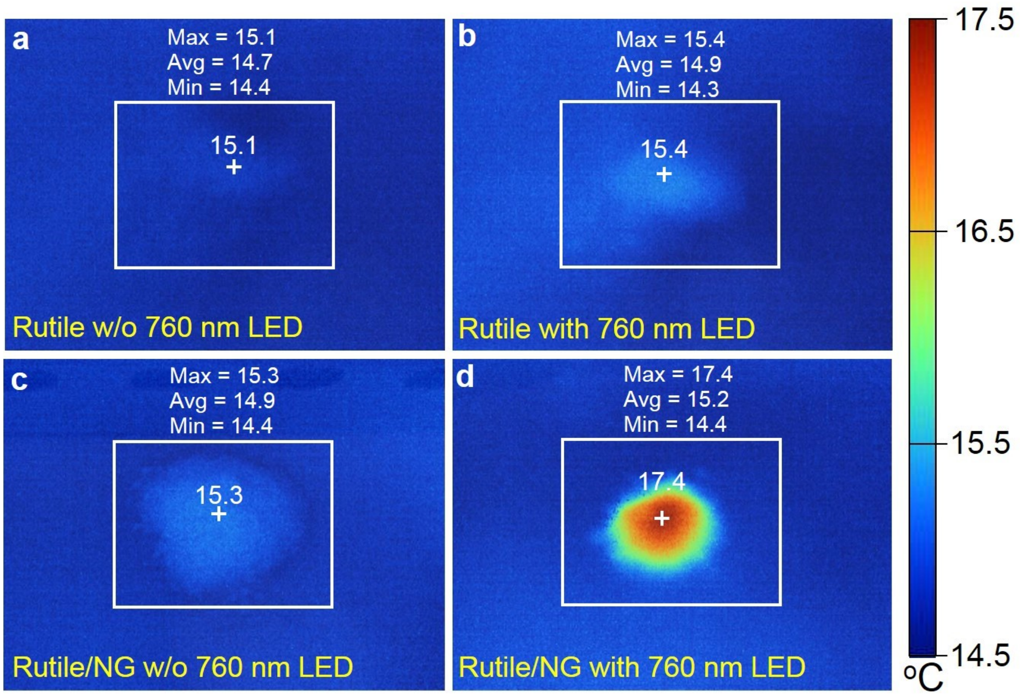

Figure S10. Infrared thermograms of the (a,b) rutile without (a) and with (b) 760 nm light irradiation, and (c,d) rutile/NG without (c) and with (d) 760 nm light irradiation.

Infrared thermogram characterization is applied to investigate the photothermal effect on the prepared samples. Obviously, no noticeable change can be observed on the rutile sample before and after 760 nm irradiation. This result is because the rutile can only absorb the incident light with a wavelength less than 400 nm. In contrast, the rutile/NG exhibits an increase in surface temperature up to 2.1 °C due to its extended light absorption range endowed by the loading of NG.[14]

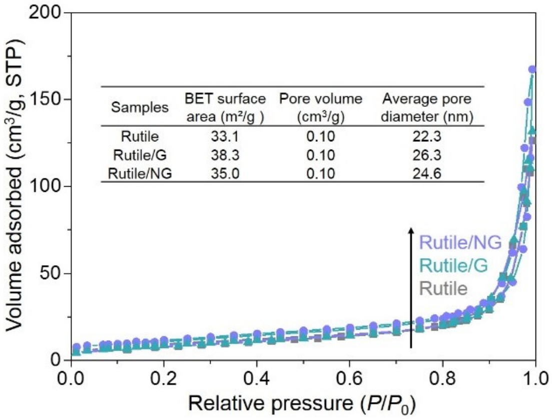

Samples	BET surface area (m²/g)	Pore volume (cm³/g)	Average pore diameter (nm)
Rutile	33.1	0.10	22.3
Rutile/G	38.3	0.10	26.3
Rutile/NG	35.0	0.10	24.6

Figure S11. Nitrogen adsorption-desorption spectra for the prepared samples. (inset) Comparison of the S_{BET}, pore volume and average pore diameter of the prepared samples.

The nitrogen adsorption–desorption technique is performed to determine the physical properties of the prepared samples including Brunauer–Emmet–Teller (BET) surface area and pore size. The nitrogen adsorption–desorption isotherms of the prepared samples and their corresponding pore-size distribution curves are shown in Figure S11. According to the Brunauer-Deming-Deming-Teller (BDDT) classification[15] type-IV isotherms are formed on nitrogen adsorption–desorption isotherms of all prepared samples, indicating the presence of mesopores (2–50 nm). In addition, H3 hysteresis loops can be observed on their isotherms at the higher relative pressure range (at the range 0.8–1.0) due to the presence of slit-like pores. At the adsorption range approaching 1.0, high adsorption can be observed, manifesting the presence of large mesopores and macropores. Finally, the specific surface area, pore diameter and pore volume information of the prepared samples are summarized (see inset). Obviously, after loading of graphene, the specific surface area of the prepared samples is enhanced due to the large specific surface area endowed by the graphene nanosheets.[16]

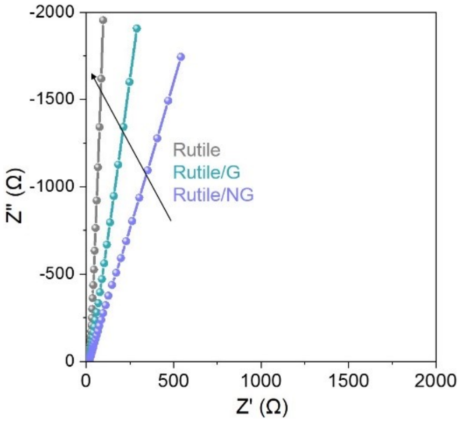

Figure S12. Nyquist plots for the prepared samples.

The electrochemical impedance spectra (EIS) characterization is also carried out to investigate the charge carrier migration process on the prepared samples. Generally, the charge carrier migration resistance of the prepared samples can be reflected by their EIS arc diameter, where the smaller arc diameter indicates the higher charge carrier separation efficiency.[17] Apparently, the rutile/NG exhibits the smallest arc diameter, manifesting its good photogenerated charge carrier separation efficiency. This superiority in photogenerated charge carrier separation is because the N-doping on the graphene can act as an intermediate transported for the photogenerated electrons due to the higher electron affinity of the N element in comparison with the C element. Specifically, under light irradiation, the photogenerated electron will first transfer from rutile to NG and then migrate from the C element to the N element on NG. Simultaneously, the photogenerated hole can be preserved on the rutile TiO_2 for the oxidation reaction. The spatial separation of photogenerated electrons and holes can allow them to be effectively utilized for the redox reaction.[18]

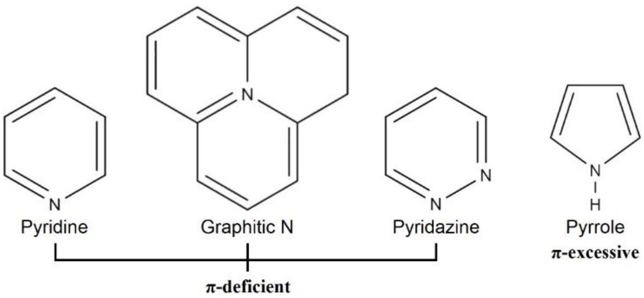

Figure S13. Comparison of the electron-withdrawing (π-deficient) and electron-withdrawing (π-excessive) properties of different N-species on NG.

The six-membered aromatics rings on the NG are π-deficient,[19] allowing them to accept photogenerated electrons from the TiO_2. The introduction of heteroatoms (i.e., nitrogen elements) into the six-membered aromatics rings can strengthen the effect and allow the intermediate photogenerated electron migration from C elements to N elements due to the higher electron affinity of N element.[20] In addition, the increase in the number of N elements can result in a higher tendency of photogenerated electrons to be accumulated on the pyridazine. It should be noted that the five-membered ring with one heteroatom (i.e., pyrrole) is π-deficient, and thus the photogenerated electrons are less likely to accumulate on pyrrole.

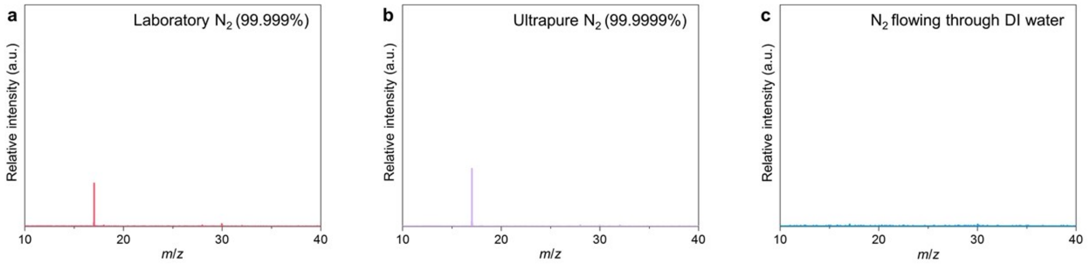

Figure S14. Mass spectra of (a) laboratory N_2 with a 99.99% purity, (b) ultrapure N_2 with a 99.9999% purity and (c) reactant gas from the reactor, where the laboratory N_2 flows through DI water before entering the reactor.

We study the photocatalytic dinitrogen conversion performance of the prepared samples in the solid-gas phase instead of the widely-applied liquid phase experimental setup to imitate the actual scheme in nature. To guarantee the humidity in the reaction system, the nitrogen gas flows through the DI water before entering the reactor. Interestingly, such a procedure can also eliminate the NH_3 in N_2 feed gas, improving the accuracy of our obtained results. In detail, according to the mass spectroscopy characterization, both the laboratory N_2 and ultrapure N_2 feed gas demonstrate a peak attributed to the NH_3 (*m*/*z* = 17). In contrast, the reactant gas obtained from the reactor shows a negligible NH_3 peak, suggesting the elimination of the NH_3 from the reactant gas.

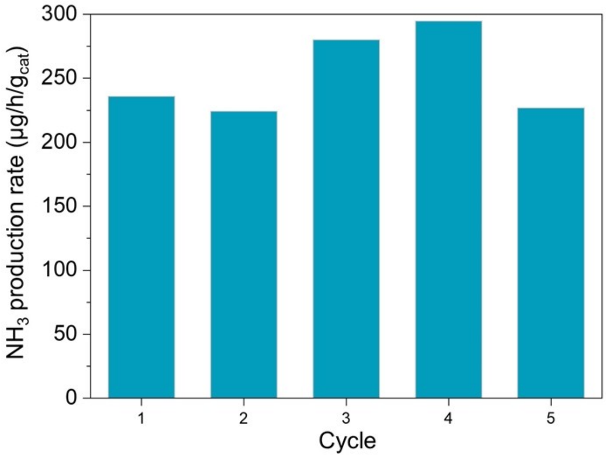

Figure S15. Recycling photocatalytic dinitrogen conversion performance for rutile/NG.

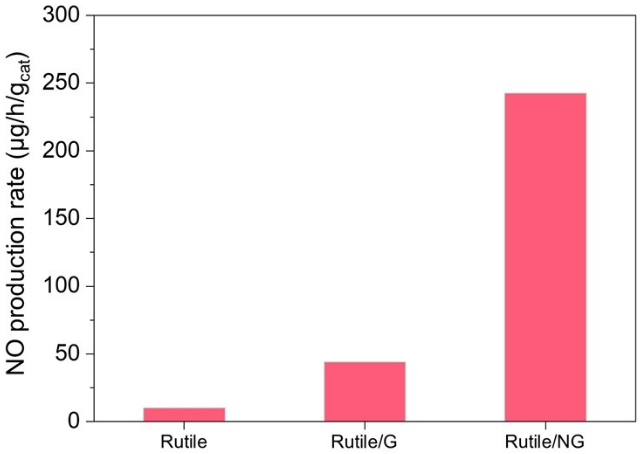

Figure S16. Comparison of the photocatalytic dinitrogen conversion performance of the prepared samples for NO production.

Unlike conventional liquid-phase reactions, our experimental design introduces water vapor into the system to supply H_2O, resulting in a relatively low H_2O concentration. Consequently, the reaction system exhibits minimal tendency for nitrite/nitrate formation. This is further supported by in situ DRIFTS measurements, where a distinct N–OH signal was observed, which is a key intermediate in NO generation. The formation of N–OH is intrinsically linked to the water activation process. Specifically, during NH_3 synthesis, H_2O undergoes dissociation to form H^+ and OH^- species. The H^+ reacts with one nitrogen moiety, transforming into NH_3, while the OH− binds to another nitrogen site to form N–OH. This N–OH intermediate subsequently undergoes dehydrogenation to ultimately yield NO.

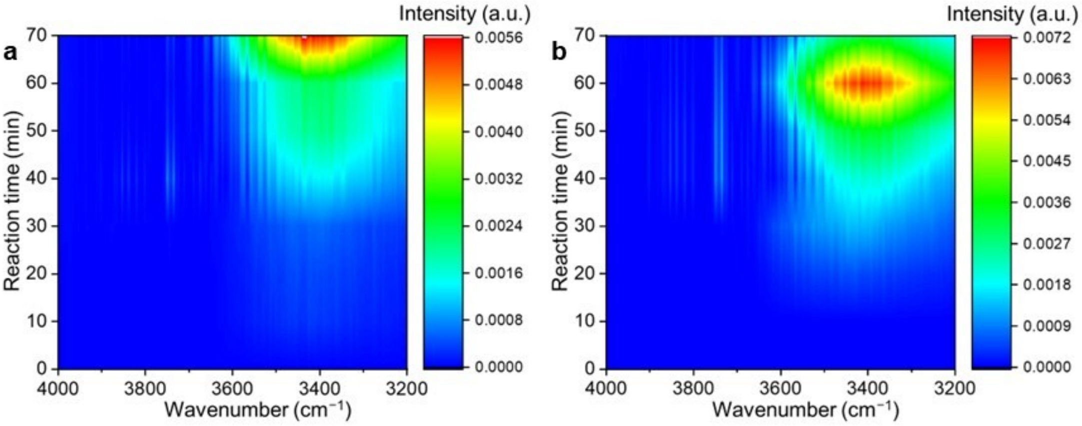

Figure S17. Contour plots for the in situ DRIFTS spectra of photocatalytic nitrogen fixation at the range of 4000–3200 cm^{-1} using rutile/NG under (a) dinitrogen/water vapor and (b) argon/water vapor flow.

The contour plots for the in situ DRIFTS spectra of photocatalytic nitrogen fixation at the range of 4000–3200 cm^{-1} using rutile/NG under dinitrogen/water vapor and argon/water vapor flow reveal distinct variation trends in the NH_3-related peak. Specifically, under dinitrogen/water vapor conditions, the NH_3-associated peak gradually intensifies, indicating an increase in the surface density of NH_3. In contrast, under argon/water vapor conditions, the NH_3 peak shows a slight decrease after 60 min of reaction. This phenomenon arises because the nitrogen dopants in NG are almost completely converted to NH_3 within 60 min, and subsequent desorption of NH_3 from the photocatalyst surface leads to the reduction in peak intensity.

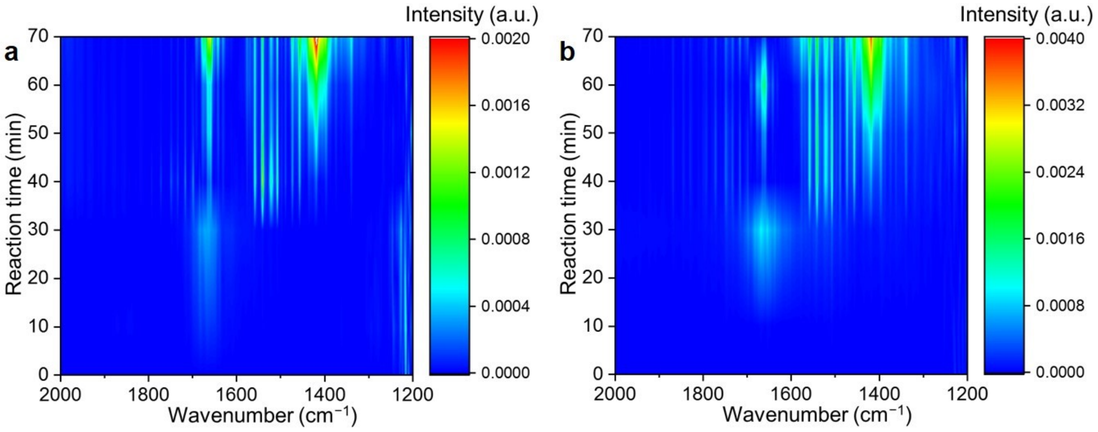

Figure S18. Contour plots for the in situ DRIFTS spectra of photocatalytic nitrogen fixation at the range of 2000–1200 cm^{-1} using rutile/NG under (a**)** dinitrogen/water vapor and (b) argon/water vapor flow.

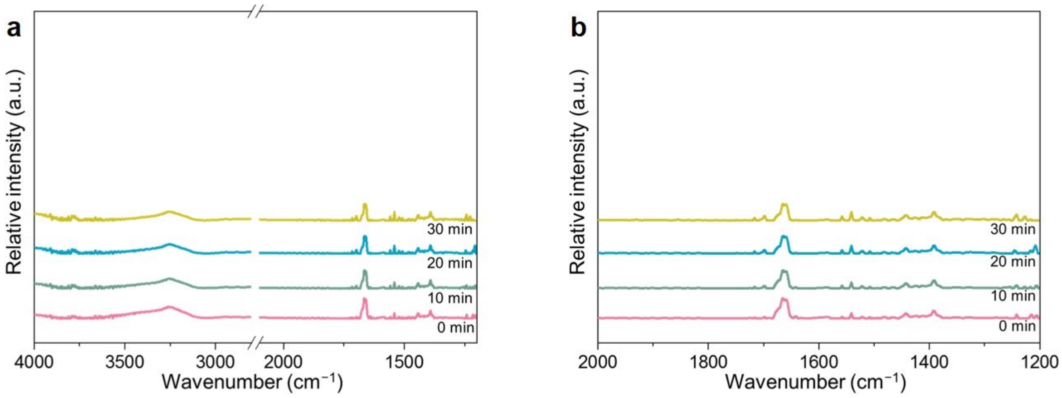

Figure S19. (a) In situ DRIFTS spectra and (b) corresponding magnified spectra of photocatalytic nitrogen fixation (365 nm LED irradiation) using rutile under dinitrogen/water vapor flow.

No significant peak attributed to the NH_3 could be observed in the in situ DRIFTS by using rutile, suggesting the negligible photocatalytic performance of rutile toward nitrogen fixation. Besides, the peaks of the samples at 1200–2000 cm^{-1} are kept almost unchanged for 30 min of light irradiation, implying the weak interaction of the surface functional groups of rutile with the N_2 gas.

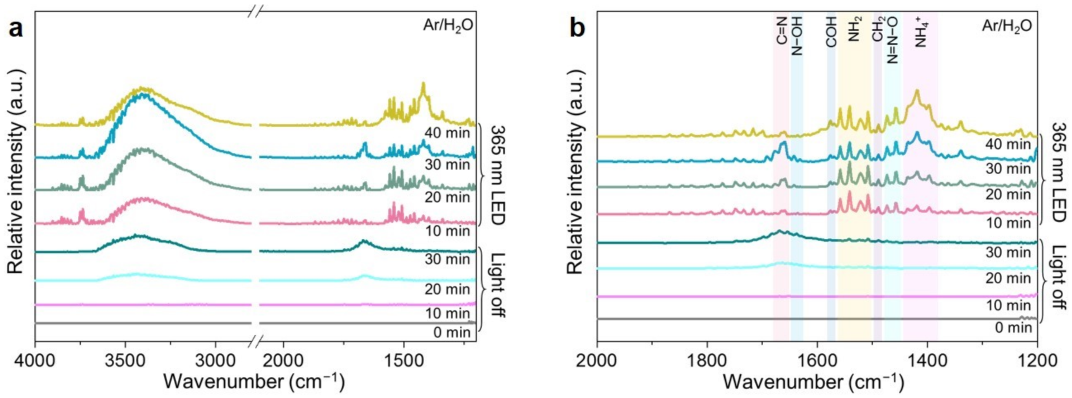

Figure S20. (a) In situ DRIFTS spectra and (b) enlarged in situ DRIFTS spectra of photocatalytic nitrogen fixation using rutile/NG under argon/water vapor flow.

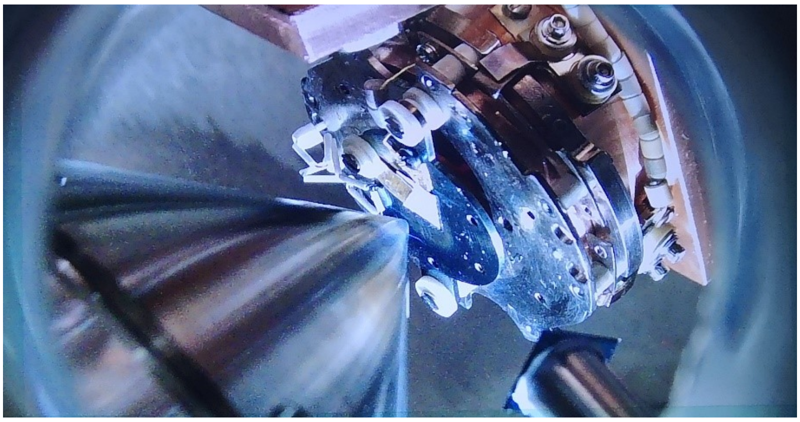

Figure S21. Optical image for the experimental setup for the NAP-XPS.

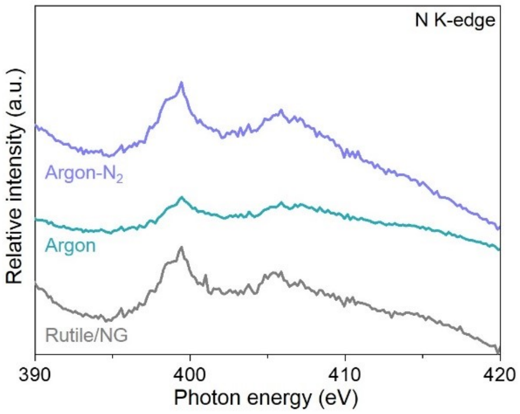

Figure S22. XAFS spectra for the rutile/NG after photocatalytic test under argon gas flow and argon-dinitrogen gas flow.

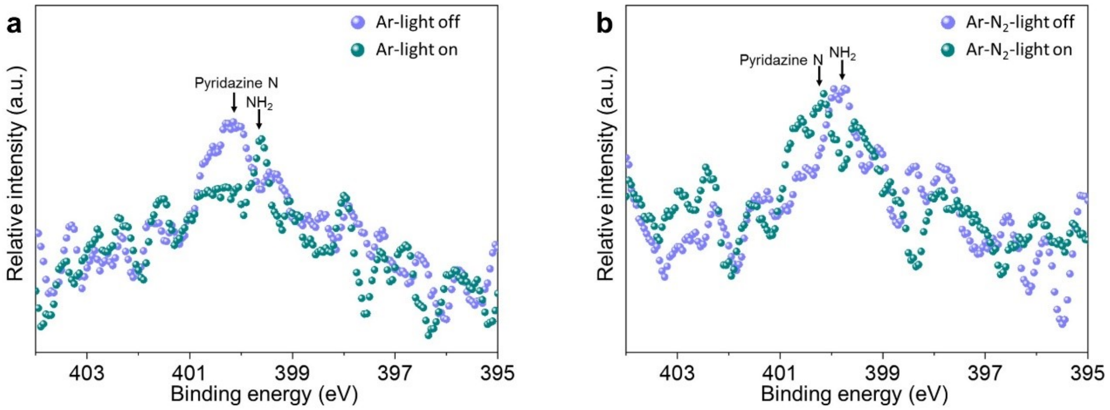

Figure S23. (a) In situ NAP-XPS spectra for the rutile/NG under Ar and H_2O atmosphere with (light on) and without (light off) light irradiation. (b) In situ NAP-XPS spectra for the rutile/NG after working in anazotic condition under N_2 and H_2O atmosphere with (light on) and without (light off) light irradiation.

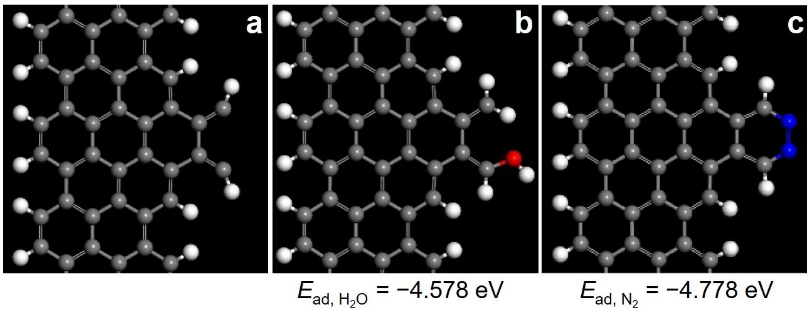

Figure S24. Electronic structures for the (a) C-diradicals, (b) adsorption of H_2O on C-diradicals and (c) adsorption of N_2 on C-diradicals on NG after removal of N-dopant.

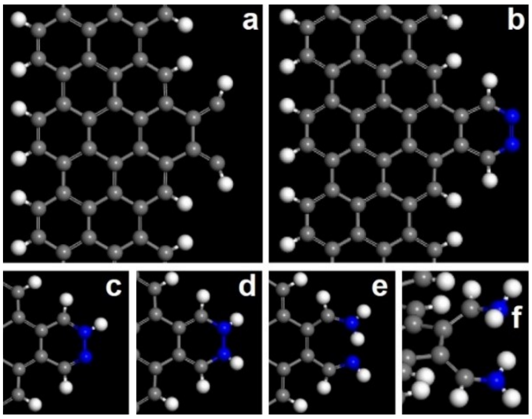

Figure S25. Schematic illustration for the structures of intermediates on the site A of NG.

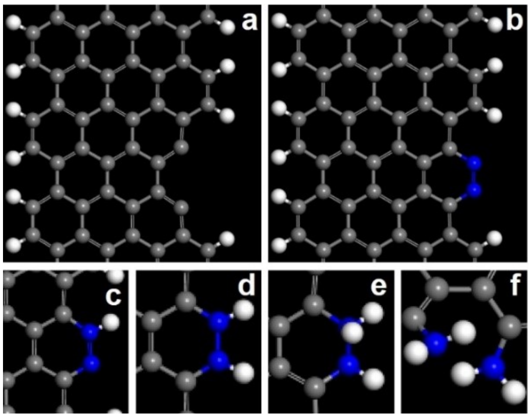

Figure S26. Schematic illustration for the structures of intermediates on the site B of NG.

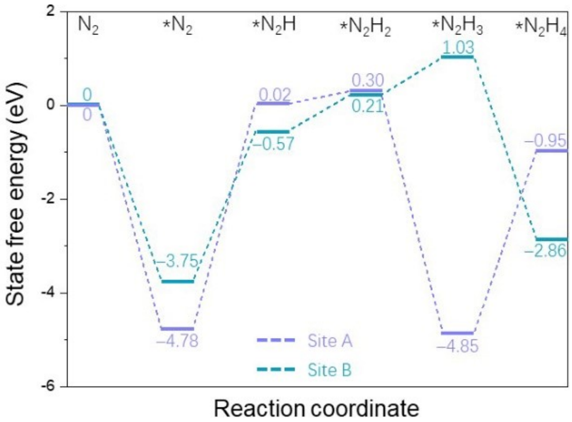

Figure S27. Free energy diagram for associative alternating dinitrogen reduction on different C*-radical structures.

Reference

1. K. Xie, X. Qin, X. Wang, Y. Wang, H. Tao, Q. Wu, L. Yang and Z. Hu, *Adv Mater*, 2012, **24**, 347–352.
2. S. Some, Y. Kim, Y. Yoon, H. Yoo, S. Lee, Y. Park and H. Lee, *Sci Rep*, 2013, **3**, 1929.
3. Y. Yang, Z. Y. Lun, G. L. Xia, F. C. Zheng, M. N. He and Q. W. Chen, *Energy Environ Sci*, 2015, **8**, 3563–3571.
4. E. T. Kang, K. G. Neoh, K. L. Tan and B. T. G. Tan, *Synthetic Met*, 1989, **31**, 79–94.
5. F. Bentiss, F. Gassama, D. Barbry, L. Gengembre, H. Vezin, M. Lagrenee and M. Traisnel, *Appl Surf Sci*, 2006, **252**, 2684–2691.
6. G. Vall-llosera, B. Gao, A. Kivimaeki, M. Coreno, J. A. Ruiz, M. de Simone, H. Agren and E. Rachlew, *J Chem Phys*, 2008, **128**, 044316.
7. T. J. Houser, M. E. McCarville and T. Biftu, *Int J Chem Kinet*, 1980, **12**, 555–568.
8. Y. Z. Xue, B. Wu, L. Jiang, Y. L. Guo, L. P. Huang, J. Y. Chen, J. H. Tan, D. C. Geng, B. R. Luo, W. P. Hu, G. Yu and Y. Q. Liu, *J Am Chem Soc*, 2012, **134**, 11060–11063.
9. Y. Ito, C. Christodoulou, M. V. Nardi, N. Koch, H. Sachdev and K. Mullen, *ACS Nano*, 2014, **8**, 3337–3346.
10. Y. Yamada, J. Kim, S. Matsuo and S. Sato, *Carbon*, 2014, **70**, 59–74.
11. Y. Yang, J. Kim, C. Kim, A. Seong, O. Kwon, J. H. Lee, I. Kristanto, L. Zhang, J. Zhou, J.-Q. Wang, J.-B. Baek, S. K. Kwak and G. Kim, *Nano Energy*, 2020, **76**, 105114.
12. G. Wang, J. Zhang, S. Hou, W. Zhang and Z. Zhao, *Nanoscale*, 2016, **8**, 9676–9681.
13. J. G. Yu, J. Jin, B. Cheng and M. Jaroniec, *J Mater Chem A*, 2014, **2**, 3407–3416.
14. C. Bie, B. Zhu, F. Xu, L. Zhang and J. Yu, *Adv Mater*, 2019, **31**, 1902868.
15. K. S. W. Sing, D. H. Everett, R. A. W. Haul, L. Moscou, R. A. Pierotti, J. Rouquerol and T. Siemieniewska, *Pure Appl Chem*, 1985, **57**, 603–619.
16. Q. Li, B. Guo, J. Yu, J. Ran, B. Zhang, H. Yan and J. R. Gong, *J Am Chem Soc*, 2011, **133**, 10878–10884.
17. Q. W. Huang, S. Q. Tian, D. W. Zeng, X. X. Wang, W. L. Song, Y. Y. Li, W. Xiao and C. S. Xie, *ACS Catal*, 2013, **3**, 1477–1485.
18. G. Lui, J. Y. Liao, A. S. Duan, Z. S. Zhang, M. Fowler and A. P. Yu, *J Mater Chem A*, 2013, **1**, 12255–12262.
19. A. R. Katritzky, C. W. Rees and E. F. Scriven, *Comprehensive heterocyclic chemistry II*, Pergamon, 1996.
20. C.-T. Hung, N. Yu, C.-T. Chen, P.-H. Wu, X. Han, Y.-S. Kao, T.-C. Liu, Y. Chu, F. Deng, A. Zheng and S.-B. Liu, *J Mater Chem A*, 2014, **2**, 20030–20037.